journal

Effect of Microstructure on Dynamic Failure Resistance of Titanium Diboride/Alumina Ceramics

Andrew R. Keller and Min Zhou

The George W. Woodruff School of Mechanical Engineering, Georgia Institute of Technology,
Atlanta, Georgia 30332-0405

The dynamic compressive strength and microscopic failure behavior of TiB_2/Al_2O_3 ceramic composites with a range of microstructural morphologies and size scales are analyzed. A split Hopkinson pressure bar is used to achieve loading rates of the order of 400 s^{-1}. The time-resolved analysis of the mechanical response is conducted with a resolution of 500 ns. The dynamic compressive strengths of the materials are 4.3–5.3 GPa, indicating a dependence of strength on microstructure. Microstructures with finer phases as measured by linear intercept length have higher strength levels. The dynamic strength levels are ~27% higher than the values of 3–4 GPa measured at quasi-static loading rates for these materials. These strength levels are also higher than the strength levels of monolithic TiB_2 and Al_2O_3 under similar dynamic conditions. A soft recovery mechanism in the experimental configuration allows the specimens to be subjected to loading under a single, well-defined stress pulse. Scanning electron microscopy and energy dispersive spectrometry indicate that failure associated with the Al_2O_3 phase is transgranular cleavage in all microstructures. On the other hand, failure associated with the TiB_2 phase is a combination of transgranular cleavage and intergranular debonding and varies with the microstructures. Quantitative image analysis shows that the measured compressive strength of the materials directly correlates with the fraction of TiB_2-rich areas on fracture surfaces. The size distribution of the fragments is quantified using digital image analysis. Comparisons of the measured distributions with the predictions of several theories suggest that the lack of accounting for microstructural characteristics contributes to the inaccuracies of the models.

I. Introduction

HIGH-PERFORMANCE ceramics possess many desirable properties that contribute to their increasing use in areas previously dominated by metals and metallic alloys. Examples of such applications include cutting tools, drill bits, wear parts, structural and electronic components, electrodes, biomechanical devices, lightweight armor, and gas-turbine components. Ceramics are well suited for such applications because of their excellent mechanical properties at high temperatures, high strength, excellent chemical stability, as well as creep, wear, oxidation, and impact resistance (Bart and Linberg[1]). Unfortunately, in addition to their attractive properties, ceramics are also characterized by a brittle nature, which can potentially lead to sudden and catastrophic failure.

Becher[2,3] has reported that transformation toughening and reinforcement processes are two approaches that can result in improved fracture toughness. Extensive research has been conducted to characterize and improve the failure resistance of ceramics, including that by Lankford,[4] Brockenbrough et al.,[5] Longy and Cagnoux,[6] Kishi et al.,[7] Curtin,[8] Shockey et al.,[9] Suresh et al.,[10] Yang and Kobayashi,[11] Evans,[12] Kishi,[13] Kobayashi,[14] Espinosa and Barr,[15] Vekinis et al.,[16] Lankford,[17] Woodward et al.,[18] Ravichandran and Subhash,[19] Chen and Ravichandran,[20] Bhattacharya et al.,[21] and Subhash and Ravichandran.[22] Some models are continuum damage theories in which the net effect of fracture is idealized as a degradation of the elasticity modulus, e.g., those of Seaman et al.,[23] Curran and co-workers,[24,25] Rajendran,[26] Johnson and Holmquist,[27] and Espinosa and Barr (1992).[15] The early work of Rose[28,29] focuses on the effect of crack size and microcracks on fracture toughness. Budiansky and co-workers[30,31] have analyzed the strength and toughness of fiber-reinforced and particulate-reinforced ceramic composites. Marshall and co-workers[32–34] have analyzed microstructural strengthening effects and failure mechanisms. Krstic[35] has studied the effect of grain size on fracture strength of brittle materials. Evans[36] and Evans and co-workers[37,38] have provided extensive analyses of the microstructural toughening and interfacial effects in ceramic composites. Curtin[39,40] has conducted experimental and analytical studies on the strength and deformation of fibrous ceramic composites. Sun et al.[41] have characterized the effects of grain shape and size on the fracture toughness of Si_3N_4. Lawn et al.[42] and Lawn[43] have presented studies on failure and microstructural effects under quasi-static and cyclic conditions. Wiederhorn et al.[44,45] have provided systematic characterization of the deformation and reliability of ceramics at high temperatures. Significant influence of microstructural effects on properties has been reported. For example, Niihara et al.[46] have reported that a 5% population of SiC nanoparticles increases the tensile strength of Si_3N_4 from 350 MPa to 1 GPa and improves its fracture toughness from 3.25 to 4.7 MPa·m$^{1/2}$. Becher[2] has demonstrated that crack-bridging toughening processes can be combined with other bridging mechanisms and with other toughening mechanisms to achieve synergistic effects. Microstructure-induced, size-dependent toughening mechanisms at the micro and nano levels are demonstrated approaches for property enhancement. To develop more-advanced materials, it is necessary to characterize the influences of phase morphology, phase length scale, and interfacial behavior on fracture toughness. Recently, two-phase ceramics of titanium diboride/alumina (TiB_2/Al_2O_3) with a range of phase sizes and phase morphologies have been developed (Logan[47,48]); these materials have shown a wide range of fracture toughness values, and some of the values are higher than those of both constituents produced separately in bulk. These materials provide an opportunity to study the correlation between microstructure and mechanical behavior.

In many applications, intensive dynamic loading occurs under normal operating conditions. Examples include particle impact on ceramic turbine blades (Bilek et al.,[49]), contact of high-speed cutting tools with a workpiece (Komanduri[50]), and impact of ballistic projectiles with ceramic armor (Anderson and Morris[51]).

The dynamic behavior of materials can be dramatically influenced by microstructural characteristics, including phase size, phase morphology, composition, and texture (Viechnicki *et al.*[52]). Thus, it is crucial to develop intrinsic relationships between fabrication, resulting microstructure, and dynamic properties to tailor ceramic systems to the needs of applications (Bilek and Helesic[49]). To establish the relationships, various processing approaches have been used to produce two-phase TiB_2/Al_2O_3 composites with four different biased microstructures. These microstructures are analyzed in this research.

II. Materials

The materials are produced through self-propagating high-temperature synthesis and mechanical mixing of powders followed by hot pressing (Logan[48] and Carney[53]). Each material has a nominal composition of 70% Al_2O_3 and 30% TiB_2 by weight. Figure 1 shows the microstructures of the four Al_2O_3/TiB_2 composites analyzed. The light areas are TiB_2 and the dark areas Al_2O_3. The microstructures vary in phase distribution and length scales. The microstructure in Fig. 1(a) shows intertwining of Al_2O_3 and TiB_2. The microstructure is unique in that its complicated morphology precludes the identification of simple crack paths through each phase or along phase interfaces. The microstructure in Fig. 1(b) consists of a dispersed TiB_2 phase and an Al_2O_3 matrix. The microstructure in Fig. 1(c) consists of Al_2O_3 matrix islands partially surrounded by a network of TiB_2 reinforcement. The matrix areas are ~20 $\mu m \times 100$ μm in size. A dispersion of nanometer-sized Al_2O_3 particles are scattered in the TiB_2 phase. Clearly, two length scales are operative in this microstructure, influencing its strength and fracture toughness. The microstructure in Fig. 1(d) is similar to that in Fig. 1(b) except for significantly larger TiB_2 phase sizes. The average TiB_2 three-dimensional phase size is 5–10 μm in Fig. 1(d) and is clearly smaller in Fig. 1(b). The smallest particles in Fig. 1(b) are of submicrometer sizes. To quantify the various phase morphologies and sizes, the linear intercept length (LIL) for the two phases is measured on digital images of the microstructures. The average values and the corresponding standard deviation are summarized in Table I. In the analysis reported here, the average LIL is used as a measure of phase size. Although there is a large variation of phase size for each microstructure, as indicated by the standard
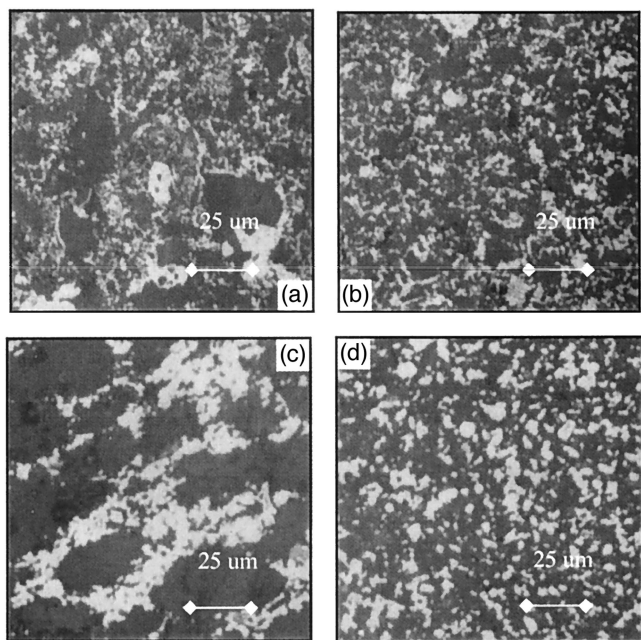
Table I. Characterization of Phase Size and Morphology

| | Linear intercept length (μm) | |
Microstructure	TiB_2	Al_2O_3
A	5.06 ± 5.33	10.30 ± 11.08
B	2.43 ± 2.45	5.88 ± 5.86
C	11.31 ± 14.89	24.77 ± 35.62
D	3.09 ± 2.75	8.17 ± 8.72

deviation of the LIL shown in Table I, the phase size difference among the microstructures is real. This difference also can be quantified, for example, by using the sum of the mean and the standard deviation of the LIL, in addition to using the mean alone.

Edirisinghe,[54] Logan,[47,48] and Carney[53] have compared the quasi-static response of these materials with those of hot-pressed Al_2O_3 and TiB_2. An $\sim30\%$ difference in fracture toughness and modulus of rupture occurs among the four materials. Kennedy *et al.*[55] have analyzed the dependence of the Hugoniot elastic limit (HEL) and spall strength on microstructure. Using a cohesive finite-element method (CFEM), Zhai and co-workers[56–59] and Zhai[60] also have quantified the effect of microstructure on energy release rate for the materials analyzed here.

III. Experimental Procedure

To characterize the response of the materials to dynamic compressive loading, a split Hopkinson pressure bar (SHPB) apparatus, as illustrated in Fig. 2, is used. This experimental apparatus permits time-resolved analyses of material response to transient compressive loading. The duration of the loading pulse is ~250 μs. A detailed discussion of this apparatus is given by Follansbee.[61] Soft recovery of specimens is achieved through the use of a momentum-trapping technique developed by Nemat-Nasser and co-workers.[62,63] This mechanism allows specimens to be recovered after loading under a single stress pulse, eliminating any unintended reloading. The specimen fragments are collected for postmortem analysis and characterization of microscopic failure. A pair of WC platens is placed between the specimen and the steel bars to prevent the bar ends from being indented. These platens have a diameter of 0.75 in. (1.9 cm) (the same as the incident and transmission bars) and a thickness of 0.125 in. (32 mm). The platens remain fully elastic and sustain no damage during the experiments. Theoretically, the somewhat different impedances of the bars and the platens may result in wave reverberations between the bars and the platens. This issue is effectively eliminated through the use of gradually increasing loading pulses generated by a pulse shaper illustrated in Fig. 2.
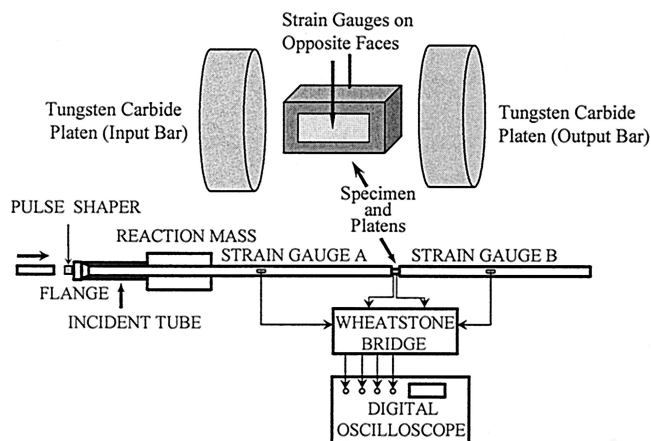

Fig. 1. Microstructures of materials analyzed (TiB_2 is light, Al_2O_3 is dark).

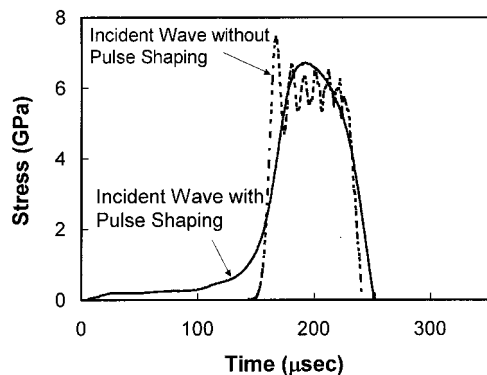Fig. 2. Schematic illustration of the experimental configuration.

Fig. 3. Incident loading pulse with gradual increase of stress.

One such loading pulse is shown in Fig. 3. The increase in time is ~150–200 μs, which is much longer than the round-trip time of 1 μs for one wave reverberation in the platens. Two strain gauges are mounted on opposite faces of the specimen to measure its strain, allowing direct determination of the strain rate and failure strain in the specimens. Figure 4 shows the strain histories for a specimen with microstructure A. The strain at which failure occurs can be easily ascertained. In general, the specimen stress is calculated using signals from strain gauges mounted on the transmission bar (see Follansbee[61]). The strain gauges mounted on the specimens also allow the accuracy of the stress measurement to be determined. Figure 5 shows a comparison of stress history determined from the transmission bar signal and the history determined from the specimen gauge signals. This particular specimen remains elastic during loading, making it possible to calculate the stress by multiplying the specimen strain by the Young's modulus of the specimen material. The excellent agreement confirms that the slowly increasing loading pulse in Fig. 3 effectively eliminates possible effects of the slight impedance mismatch between the bars and the platens. More details of the experiments are given in Keller.[64]

IV. Postmortem Microscopic Analysis

Scanning electron microscopy (SEM) is used to characterize the microscopic fracture behavior of the materials. Energy dispersive spectrometry (EDS) is used to identify the Al_2O_3-rich and TiB_2-rich areas. Digitized EDS dot maps are analyzed to determine the fractions of the fracture surfaces that are within each phase and along the interphase interfaces. Distribution of fragment sizes is characterized through the quantification of fragment mass. Two methods are used. The first involves the direct measurement of the mass of each particle using a scale (Model AJ100, Mettler, Toledo, OH). The second involves the use of digital images of recovered fragments. The volume of each fragment is estimated based on the
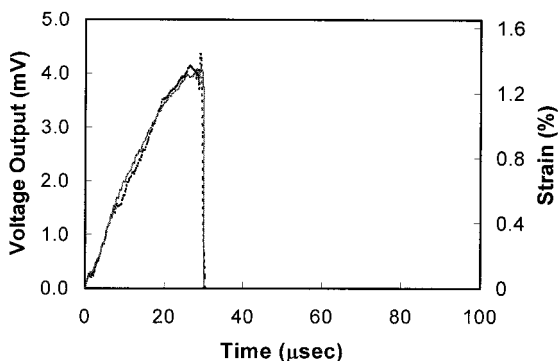

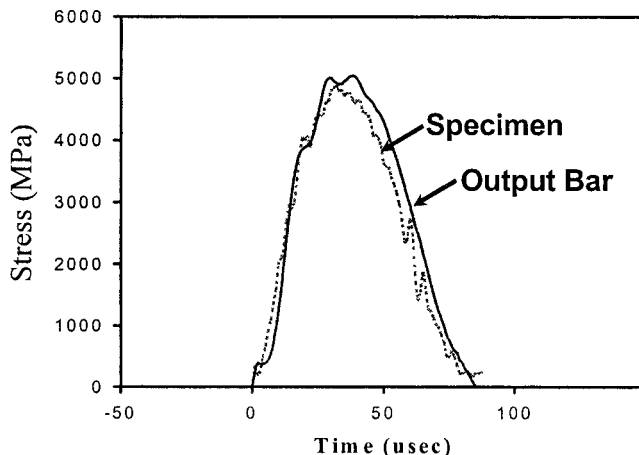**Fig. 4.** Measured histories of specimen strains (microstructure A).

Fig. 5. Comparison of stress histories from specimen and bar measurements.

assumption of a spherical shape for each particle. The mass is then calculated using the density of each material. The second approach provides a better particle-size resolution than the first method. Because the minimum fragment mass that can be accurately measured is 0.001 g, smaller fragments that are left unaccounted for in the direct measurement are included in the digital image analysis, thus yielding a more complete quantification of the fragment-size distribution.

V. Compressive Strength

The time histories of stress carried by specimens of the four materials during gradual compressive loading are shown in Fig. 6. The loading pulse is 250 μs, significantly longer that the response periods shown. Clearly, failure occurs for all specimens, and the decrease in stress is due to the loss of stress-carrying capability, not unloading. Multiple specimens are analyzed for each material. The maximum stress on each curve is taken as the compressive strength for the corresponding specimen. The distributions of the strength for the four materials are shown in Fig. 7. There is a clear difference in the average value and the range of variation.

Microstructure A is characterized by a morphology with relatively large islands of Al_2O_3 surrounded by continuous bands of TiB_2. The specimens of this material have an average density of 4.10 g/cm^3, which is 99% of the theoretical density of 4.14 g/cm^3 for a material with 70% Al_2O_3 and 30% TiB_2 by weight. The average failure stress is 5.2 GPa, and the average failure strain is 1.2% ± 0.9%. The experiments have an average strain rate of 334 s^{-1}. The specimens show a range of rates in the loss of load-carrying capability following the peak load, between 5 and 45 μs, with the majority within 5–15 μs. Lower rates of stress decrease can be used as an indication of less rapid or catastrophic failure process.

Microstructure B is characterized by homogeneously distributed TiB_2 particles within a matrix of Al_2O_3. The average density is 3.95 g/cm^3, which is 95% of the theoretical density. The average failure stress is 4.7 GPa, and the average failure strain is 1.21% ± 0.21%. The average strain rate in the experiments is 426 s^{-1}. The specimens tested display more rapid losses of the load-carrying capability (5–15 μs) than those made of microstructure A. The lower strength also coincides with smaller fragments compared with microstructure A. The lower strength and the propensity for sudden, catastrophic failure shown by the specimens tested can be primarily attributed to the relatively higher levels of porosity in this microstructure, rather than its morphology. Because this microstructure is the only material with a low density among the four materials analyzed, the comparison for microstructural morphology effects focuses primarily on the other three microstructures.
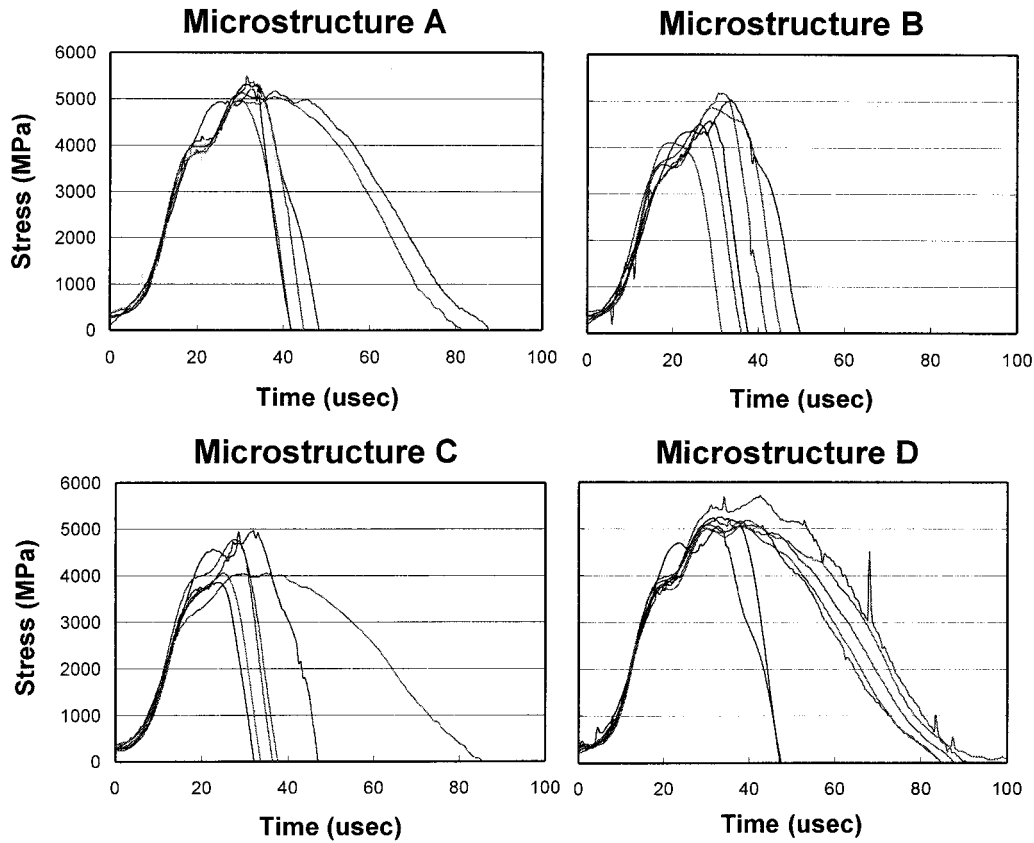
Fig. 6. Stress histories.

Microstructure C consists of relatively large islands of Al_2O_3 surrounded by continuous, interconnected bands of TiB_2. This material has a density of 4.11 g/cm^3, or 99% of the theoretical density. The average failure stress is 4.4 GPa, and the average failure strain is 1.12% ± 0.20%. The average strain rate in these experiments is 412 s^{-1}. The majority of the specimens for this microstructure show relatively more rapid loss (within 5–12 µs) of load-carrying capability following the peak stress.

Microstructure D has a morphology similar to that of B but with much larger TiB_2 particle sizes. This material has an average density of 4.10 g/cm^3, or 99% of the theoretical value. The average failure stress is 5.2 GPa, and the average failure strain is 1.18% ± 0.09%. The average strain rate in these experiments is 323 s^{-1}. The specimens show relatively low rates in the loss of load-carrying capability, with a majority of the tested specimens requiring failure periods between 45 and 56 µs. The higher strength (and perhaps slower process of failure) indicates a stronger failure resistance compared with other materials. This is also consistent with the larger average fragments observed for this material.

Clearly, microstructures A and D show significantly higher failure resistance than microstructure C and higher resistance than microstructure B. A summary of the average densities and failure stresses are given in Fig. 8. The error bars indicate standard deviation for the stress. There is an interest in identifying microstructural factors influencing the failure behavior of the materials. Figure 9(a) shows the correlation between the compressive strength and the average LIL. Because material B has a much higher level of porosity than those of the other materials, attention is given only to materials A, C, and D. Higher strengths coincide with smaller LIL. This can be phenomenologically explained.
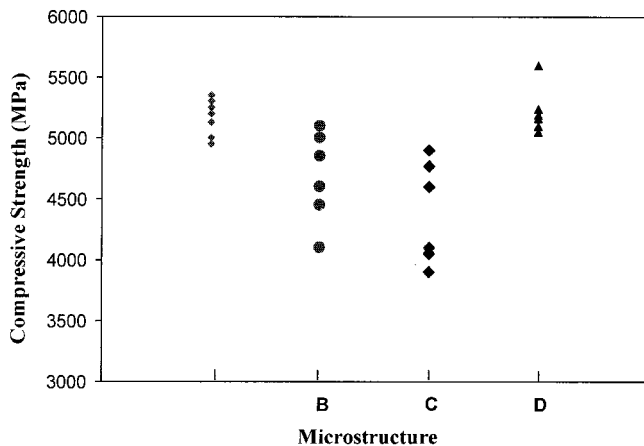
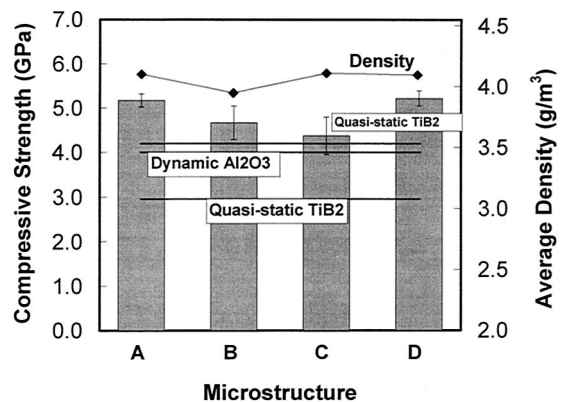

Fig. 7. Measured distribution of strength.

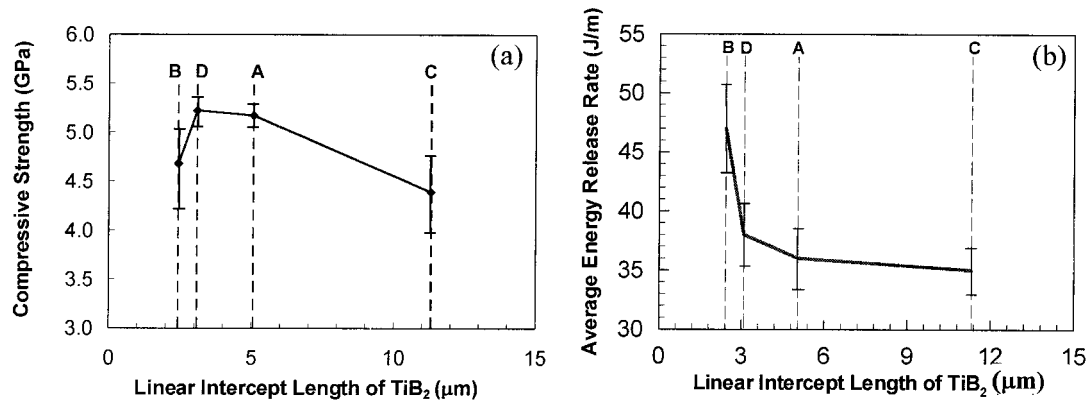**Fig. 8.** Compressive strength and density.

Fig. 9. Correlation between failure resistance and LIL: (a) measured compressive strength and (b) calculated average energy release rate.

Microstructures with smaller LIL values present a more heterogeneous media for propagating cracks, inducing more tortuous crack paths and, therefore, increasing energy dissipation for crack growth. This finding is consistent with the results of the explicit fracture modeling of Zhai *et al.*[58,59] and Zhai[60] using the same microstructures. In that work, the actual energy dissipated per unit fracture surface generated (called here the energy release rate) is used as a measure for the failure resistance of the materials. Although this energy release rate is a physical quantity different from the strength measured in the experiment, it is material dependent and is used as a relative indicator of the effects of microstructure on material failure. This use is not meant to confuse strength with energy release rate, but rather to identify trends in microstructure–failure resistance relations. The micromechanical quantification of the fracture resistance of the four microstructures accounts for the actual phase distributions and arbitrary fracture patterns. A comparison of trends for the experimentally measured strength and calculated rate of energy dissipated per unit crack surface area is given in Fig. 9, with Fig. 9(b) showing the calculated result. In the modeling, an explicit account of fracture is the pursued, using a two-dimensional microstructural representation and a plane strain formulation. Arbitrary crack paths and microcrack patterns are explicitly resolved. The approach allows fracture in each of the phases as well as along the interphase boundaries to be explicitly modeled and tracked. Because the bonding strength (in terms of separation energy and maximum stress) between the phases in the actual materials cannot be directly measured, different levels of bonding strength (weak, intermediate, and strong) between the TiB_2 and Al_2O_3 phases are assumed and analyzed in the calculations. This difference in bonding strength refers to different levels of separation energy and maximum stress required to cause separation along the phase boundaries. Details about the cohesive finite-element framework and the calculations can be found in Zhai *et al.*[58,59] and Zhai.[60] However, regardless of how strongly or weakly the two phases are bonded (e.g., as a result of processing), a common trend of increasing energy dissipated per unit crack surface area with decreasing phase size occurs. For clarity of the figure, only the result for weak bonding is shown in Fig. 9(b). This trend is consistent with the experimental trend of higher strength for small phase sizes observed in Fig. 9(a). In the modeling, porosity in microstructure B is not considered; therefore, only results from microstructures A, C, and D should be used for comparison between the calculations and the experiments. The experimental and numerical results for microstructure B are, however, significant in that they demonstrate the microstructural morphology in B is likely one that offers a strong failure resistance. Indeed, even with its higher level of porosity, microstructure B shows a higher level of strength in the experiments compared with microstructure C.

VI. Fractography

The fragments of fractured specimens are recovered and the morphologies of the fracture surfaces are analyzed. Coinciding EDS maps showing the distributions of Al_2O_3-rich and TiB_2-rich areas are taken for each region analyzed. The fractographs and the corresponding EDS maps for microstructures A and D are shown in Figs. 10 and 11. The simultaneous use of these phase maps and fractographs greatly facilitates the identification of the phases on fracture surfaces and the intergranular or intragranular nature of the fracture process. The area fractions of Al_2O_3-rich and TiB_2-rich regions are measured. The measurements are obtained on digital images of the EDS maps, representing fractions on planar projection planes. This measurement is consistent with the measurement of volume/area fractions for phases on planar sections of microstructures, allowing comparisons to be made. The measured fractions reported here are for large areas, not over the small images shown.

Figure 10 shows fracture surface areas for microstructure A. The failure process bears resemblance to the morphology of the microstructure, showing large regions of Al_2O_3 surrounded by a continuous network of TiB_2. The Al_2O_3 areas are large and smooth, indicating transgranular cleavage inside Al_2O_3 grains. The cleavage planes span over multiple grains, as indicated by the facets and ledges in Fig. 10(a). Failure involving the TiB_2 phase appears to be primarily intergranular pullout. The overall failure is a combination of transgranular cleavage inside Al_2O_3 and intergranular separation along Al_2O_3/TiB_2 boundaries: ~74% of the fracture surface is cleavage planes within the Al_2O_3 and 26% is associated with the TiB_2. The volume fraction of Al_2O_3 in this material is 72.6%.

The fracture surfaces for microstructure B are dominated by small regions of transgranular cleavage of the Al_2O_3 phase. Similar to what is seen for microstructure A, failure involving the TiB_2 phase occurs primarily by intergranular pullout. TiB_2 particles are relatively evenly distributed on the fracture surfaces, suggesting a fracture process that is not significantly affected by the presence of the particles. Also, numerous pores are observed in the Al_2O_3 phase, consistent with the measured low density (95% of theoretical value) of this material. Clearly, excessive porosity is detrimental to the resistance to crack propagation in this material: ~84% of the fracture surface is Al_2O_3-rich, significantly higher than the 72.6% volume fraction of Al_2O_3 in this material. Thus, the occurrence of fracture is predominantly in the Al_2O_3 phase. Because Al_2O_3 has a lower strength and lower fracture energy than TiB_2, this higher ratio of fracture surfaces in Al_2O_3 appears to be the primary reason for the observed low strength reported earlier.

A primarily transgranular mode of fracture inside Al_2O_3 is also observed for microstructure C. Fracture surfaces are dominated by large areas of cleavage within the Al_2O_3 phase. However, failure involving the TiB_2 phase occurs through a combination of transgranular cleavage and intergranular pullout. Most parts of the

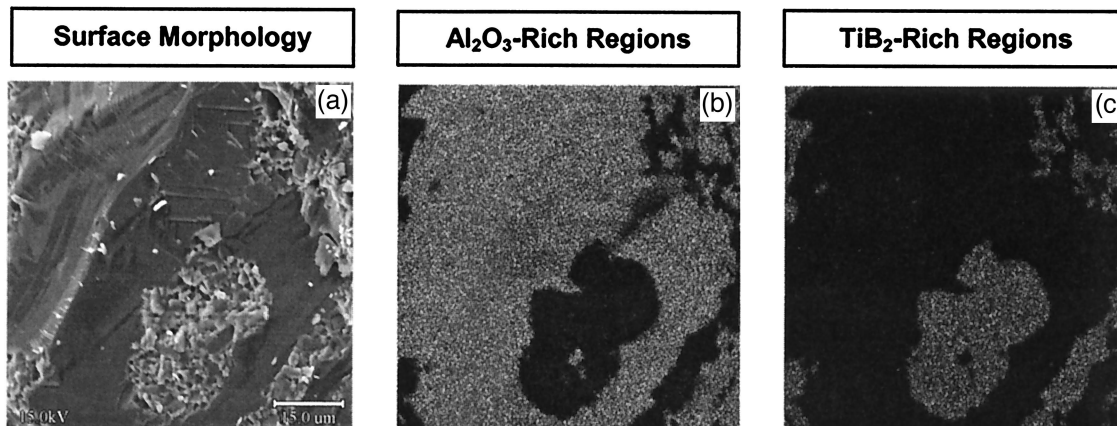| Surface Morphology | Al$_2$O$_3$-Rich Regions | TiB$_2$-Rich Regions |

Fig. 10.   SEM images of fracture surfaces after experiment, microstructure A.

fracture surfaces associated with the TiB$_2$ show intergranular pullout. The fracture surface characteristics reflect the morphology of this microstructure, i.e., large areas of cleavage in Al$_2$O$_3$ surrounded by a continuous network of TiB$_2$. The fact that cleavage in Al$_2$O$_3$ occurs over multiple grains contributes to its lower failure resistance, because the effectiveness of the TiB$_2$ as a reinforcing phase is decreased. Very few pores are observed in the Al$_2$O$_3$ phase, consistent with the measured density of 99% of the theoretical density. No pores are observed in the TiB$_2$ phase: ~77% of the fracture surface is Al$_2$O$_3$ rich, higher than the 72.6% volume fraction of Al$_2$O$_3$ in the material. Thus, there appears to be a slight preference for failure to occur in the Al$_2$O$_3$ phase.

The failure in microstructure D is unique in that transgranular cleavage is the primary fracture mechanism for Al$_2$O$_3$ and TiB$_2$ (see Fig. 11). Although failure involving the TiB$_2$ phase occurs through a combination of transgranular cleavage and intergranular pullout, the dominant mechanism is cleavage. This is in sharp contrast to what is observed for the other microstructures. Evenly distributed TiB$_2$ particles across the fracture surfaces complement the microstructural morphology of fine particles embedded in an Al$_2$O$_3$ matrix. It also appears that the homogeneous distribution of TiB$_2$ reinforcement inhibits intergranular separation, thus forcing cracks to go through the stronger TiB$_2$ phase and enhancing failure resistance. The rough and ragged nature of the surface is in contrast to the relatively smooth appearance of the surfaces for microstructures A, B, and, most prominently, C: ~71% of the fracture surface is Al$_2$O$_3$-rich, lower than the 72.6% volume fraction of Al$_2$O$_3$ in this material. This is the only microstructure that shows a TiB$_2$-rich fracture surface fraction higher than its corresponding volume fraction in the material. This bias toward the TiB$_2$ points to an unusual shift of failure into the stronger phase

and can be associated with the significantly higher strength shown in Figs. 7 and 8.

In all four microstructures, the failure of Al$_2$O$_3$ is through transgranular cleavage. The failure of TiB$_2$ is through intergranular pullout in microstructures A and B, and a combination of intergranular pullout and transgranular cleavage in microstructures C and D. For microstructures A, B, and C, Al$_2$O$_3$ accounts for at least 72.6% of the fracture surface, with B showing the greatest preference for failure in Al$_2$O$_3$, at 84%. Clearly, increasing fracture surface area in Al$_2$O$_3$ corresponds to lower strength. Microstructure D shows the lowest fraction of Al$_2$O$_3$ fracture surfaces (72.6%) among all materials analyzed. This is also the only microstructure that shows an Al$_2$O$_3$ surface fraction lower than the volume fraction of this phase. This indicates a shift of failure from the Al$_2$O$_3$ phase toward the TiB$_2$ phase, leading to the higher strength of this material.

VII.   Fragmentation Patterns

Fragmentation under dynamic conditions involves the nucleation, growth, and coalescence of a network of cracks (Grady and Kipp[65,66]). At low loading rates, unloading waves emitted from an activated crack relax stresses in nearby regions (Shockey[67]). This stress relaxation prevents further activation of smaller cracks, resulting in fewer and larger fragments. Under rapid loading, more cracks are activated because of the lack of time for stress wave propagation and stress relaxation, leading to more and smaller fragments. The fragmentation process is significantly influenced by microscopic heterogeneities and microstructure. Lienau,[68] Mott and Linfoot,[69] Grady and Kipp,[65,66] and Grady[70] have conducted

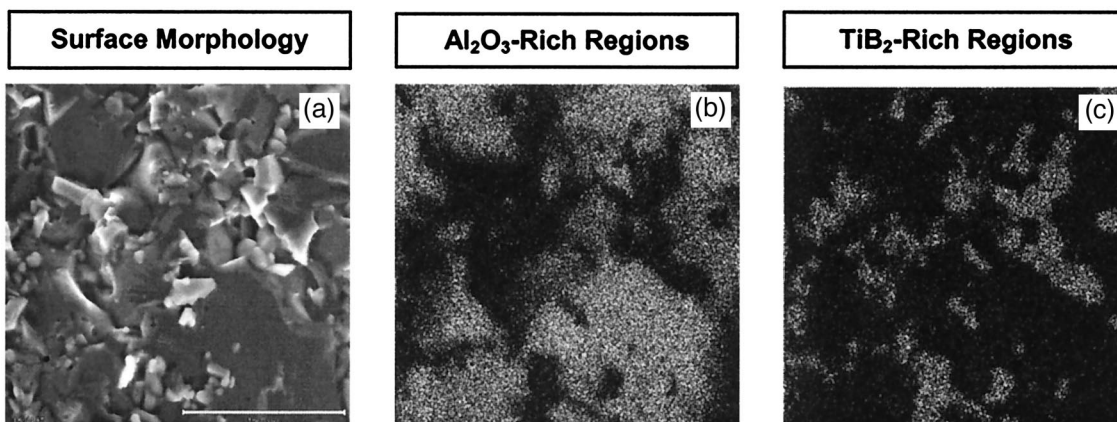| Surface Morphology | Al$_2$O$_3$-Rich Regions | TiB$_2$-Rich Regions |

Fig. 11.   SEM images of fracture surfaces after experiment, microstructure D.
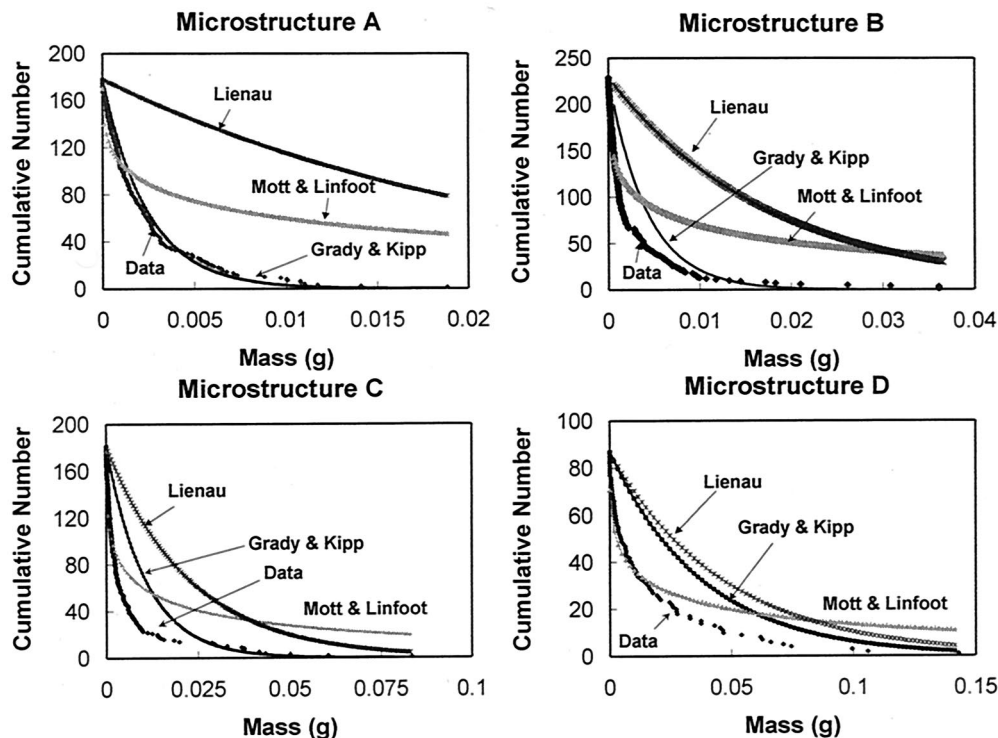
Fig. 12. Distribution of fragment size.

one-, two-, and three-dimensional characterizations of the statistical outcome of the fragmentation process.

Lienau[68] assumes that fragmentation initiates from randomly distributed flaws on a line, and the distribution of fragment lengths is determined by the distances between the flaws. This characterization has been extended to two- and three-dimensions by Grady and Kipp.[65,66] Specifically, the three-dimensional relation is

$$N(m) = N_0 \exp(-N_0 m) \qquad (1)$$

where $N(m)$ is the cumulative number of fragments with mass $>m$ and N_0 the total number of fragments. Mott and Linfoot[69] have found that the distribution of fragment size in their experiments can be more accurately described by

$$N(m) = N_0 \exp[-(3N_0 m)^{1/3}] \qquad (2)$$

Grady and Kipp[65,66] and Grady[70] have further improved the models. They assume that the probability of fracture is spatially uniform and that all points in a body are accessible to fracture, and adjacent fracture sites can be arbitrarily close to each other. In application, an event can be regarded as continuous if the average fragment size is large relative to the minimum fragment size. For the specimens analyzed here, the minimum fragment size is typically less than one-fourth of the average fragment size. Thus, the assumption of continuous fracture is valid. Under such conditions, they have obtained the following distribution function for dynamic fragmentation:

$$N(m) = N_0 \exp\left[\left(\frac{M}{\mu} - 1\right)\ln\left(1 - \frac{m}{M}\right)\right] \qquad (3)$$

where M is the total mass of the body and μ the average fragment mass.

Digital images of the recovered fragments for the four materials are used in the quantification of the fragment-size distribution for each material. The measured distributions are shown in Fig. 12 with the predictions of Eqs. (1)–(3). Except for microstructure D, the prediction of Grady and Kipp[65,66] provides the best fit to the experimental data. The best prediction is for microstructure A, which has the smallest average fragment size. As the average

fragment size increases, the accuracy of prediction by Grady and Kipp decreases, whereas the accuracy of the Mott and Linfoot[68] distribution improves. For the specimens analyzed, $M \approx 0.29$ g. The average fragment size and total number of fragments per specimen for the four microstructures are summarized in Table II. The sum of the fragment mass is $<M$. The cause of this discrepancy is a combination of two factors. The first is that the fragments range in size from dustlike particles to particles with sizes almost one-half that of the original specimen. It is virtually impossible to recover the dustlike particles on the very small side of this spectrum. This contributes to the discrepancy in the data. The second is the fact that the fragment sizes are estimated based on the projected area of each fragment. The approximation associated with this analysis contributes to the error.

As shown in Table II, microstructure D yields the largest mean fragment size. This microstructure also displays the highest compressive strength. Although it has a strength similar to that of microstructure D, microstructure A yields the smallest average fragment mass, which is similar to that of the much weaker and more porous microstructure B. Microstructure C, which has the lowest compressive strength, yields the second largest average fragment size. Therefore, it appears that no direct correlation exists between the measured strength and average fragment size for the materials and conditions analyzed.

VIII. Discussion

The analysis using four TiB_2/Al_2O_3 ceramic composites with different microstructural morphologies and size scales has yielded

Table II. Summary of Average Fragment Mass

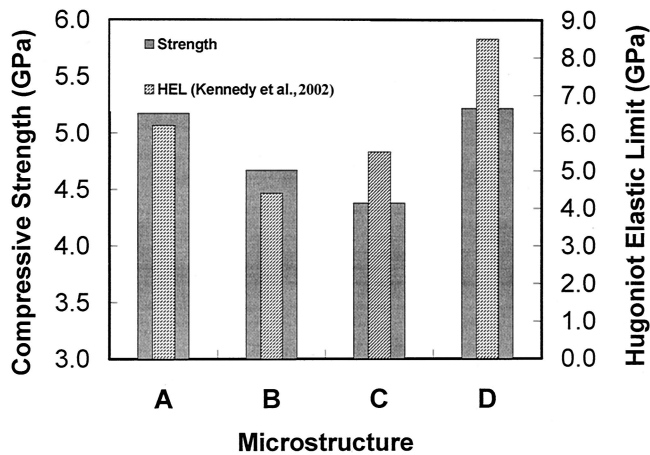| Microstructure	Average fragment mass (mg)	Average fragment count
A	2.4	46
B	3.0	60
C	5.9	46
D	18.2	22

Fig. 13. Summary of compressive strength and HEL.

dynamic compressive strength between 4.3 and 5.3 GPa, indicating a dependence of strength on microstructure. Microstructures with finer phases, as indicated by lower LIL values, have higher strength levels. This result follows the general relationship between grain size and strength (Nordgen and Melader[71] and Krstic[72]). Also, low density has a significant negative influence on strength. The dynamic strength levels are ~27% higher than the values of 3–4 GPa measured at quasi-static loading rates. SEM and EDS indicate that failure associated with the Al_2O_3 phase is transgranular cleavage in all microstructures. On the other hand, failure associated with the TiB_2 phase is a combination of transgranular cleavage and intergranular debonding and varies with the microstructures. The fraction of TiB_2-rich fracture surface areas directly correlates with the measured compressive strength of the materials. The size distributions of the fragments indicate no direct correlation between strength and average fragment size for the materials under the conditions analyzed. Comparisons of the measured distribution with the predictions of several theories suggest that the lack of accounting for microstructural characteristics contributes to the inaccuracies of existing fragmentation models.

The measured compressive strengths for the four materials are compared with those for Al_2O_3 and TiB_2 under different conditions in Fig. 8. The addition of TiB_2 reinforcement clearly improves the failure resistance of the materials. Hot-pressed monolithic Al_2O_3 has a reported compressive strength of 3.0 GPa under quasi-static loading conditions. The reported strength of hot-pressed TiB_2 is 4.2 GPa. At a strain rate of 10^3 s^{-1}, compressive strength is 3.7–4.0 GPa (Logan[47,48]). At a strain rate of 412 s^{-1}, the weakest of the four materials tested (material C) has a compressive strength of 4.4 GPa, significantly higher than those for the monolithic materials. The strength levels of the four materials are also higher than that reported for hot-pressed TiB_2 under quasi-static loading conditions.

The compressive strength reported here is for uniaxial stress conditions. The HEL can be regarded as a measure for strength under conditions of uniaxial strain. The HEL values for the materials analyzed have been obtained by Kenndy *et al.*[55] A comparison of the HEL and the compressive strength is shown in Fig. 13. There is a strong correlation between these two failure resistance measures, with microstructure D showing the highest resistance followed by microstructure A. This correlation confirms the findings on the influence of phase size and failure mechanism on failure resistance described in this paper.

References

[1]R. K. Bart and J. C. Lindberg, "Ceramic Bodyguards," *Adv. Mater. Processes*, **132** [3] 69–72 (1987).

[2]P. F. Becher, "Microstructural Design of Toughened Ceramics," *J. Am. Ceram. Soc.*, **74**, 255–69 (1991).

[3]P. F. Becher, "Advances in the Design of Toughened Ceramics," *J. Ceram. Soc. Jpn.*, **99**, 993–1001 (1991).

[4]J. Lankford, "Dynamic Compressive Fracture in Fiber-Reinforced Ceramic Matrix Composites," *Mater. Sci. Eng. A*, **A107**, 261–68 (1989).

[5]J. R. Brockenbrough, S. Suresh, and J. Duffy, "An analysis of Dynamic Fracture in Microcracking Solids," *Philos. Mag. A*, **58**, 619–34 (1988).

[6]F. Longy and J. Cagnoux, "Plasticity and Microcracking in Shock-Loaded Alumina," *J. Am. Ceramic Soc.*, **72**, 971–79 (1989).

[7]T. Kishi, N. Takeda, and B. N. Kim, "Dynamic Fracture Toughness and Microstructural Fracture Mechanisms in Ceramics," *Ceram. Eng. Sci. Proc.*, **11** [7–8] 650–64 (1990).

[8]W. Curtin, "Theory of Mechanical Properties of Ceramic-Matrix Composites," *J. Am. Ceram. Soc.*, **74**, 2837–45 (1991).

[9]D. A. Shockey, A. H. Machand, S. R. Skaggs, G. E. Cort, M. W. Burkett, and R. Parker, "Failure Phenomenology of Confined Ceramic Targets and Impact Rods," *Int. J. Impact Eng.*, **9**, 263–75 (1990).

[10]S. Suresh, T. Nakamura, Y. Yeshurun, K. H Yang, and J. Duffy, "Tensile Fracture Toughness of Ceramic Materials: Effects of Dynamic Loading and Elevated Temperatures," *J. Am. Ceram. Soc.*, **73**, 2457–66 (1990).

[11]K.-H. Yang and A. S. Kobayashi, "Dynamic Fracture Response of Alumina and Two Ceramic Composites," *J. Am. Ceram. Soc.*, **73** [8] 2309–15 (1990).

[12]A. G. Evans, "The Mechanical Properties of Reinforced Ceramic, Metal, and Intermetallic Matrix Composites," *Mater. Sci. Eng.*, **A143**, 63–76 (1991).

[13]T. Kishi, "Dynamic Fracture Toughness in Ceramic and Ceramic-Matrix Composites," *Eng. Fract. Mech.*, **40**, 785–90 (1991).

[14]A. S. Kobayashi, "Dynamic Fracture of Ceramics and Ceramic Composites," *Mater. Sci. Eng.*, **A143**, 111–17 (1991).

[15]H. D. Espinosa and N. S. Brar, "Dynamic Failure Mechanisms of Ceramic Bars: Experiments and Numerical Simulations," *J. Mech. Phys. Solids*, **43**, 1615–38 (1995).

[16]G. Vekinis, M. F. Ashby, H. Shercliff, and P. W. Beaumont, "The Micromechanisms of Fracture of Alumina and Ceramic-Based Fiber Composite: Modeling the Failure Processes," *Compos. Sci. Technol.*, **48**, 325–30 (1993).

[17]J. Lankford, "Effect of Hydrostatic Pressure and Loading Rate on Compressive Failure of Fiber-Reinforced Ceramic-Matrix Composites," *Compos. Sci. Technol.*, **51**, 537–43 (1994).

[18]R. L. Woodward, W. A. Gooch, R. G. O'Donnell, W. J. Oerciballi, B. J. Baxter, and S. D. Oattie, "A Study of Fragmentation in the Ballistic Impact of Ceramics," *Int. J. Impact Eng.*, **15**, 605–18 (1994).

[19]G. Ravichandran and G. Subhash, "Critical Appraisal of Limiting Strain Rates for Compression Testing of Ceramics in a Split Hopkinson Pressure Bar," *J. Am. Ceram. Soc.*, **77**, 263–67 (1994).

[20]W. Chen and G. Ravichandran, "Failure Mode Transition in Ceramics under Dynamic Multiaxial Compression," *Int. J. Fract.*, **101**, 141–59 (2000).

[21]K. Bhattacharya, M. Ortiz, and G. Ravichandran, "Energy-Based Model of Compressive Splitting in Heterogeneous Brittle Solids," *J. Mech. Phys. Solids*, **46**, 2171–81 (1998).

[22]G. Subhash and G. Ravichandran, "Mechanical Behaviour of a Hot-Pressed Aluminum Nitride under Uniaxial Compression," *J. Mater. Sci.*, **33**, 1933–39 (1998).

[23]L. Seaman, D. R. Curran, and W. J. Murri, "A Continuum Model for Dynamic Tensile Microstructure and Fragmentation," *J. Appl. Mech.*, **52**, 593–600 (1985).

[24]D. R. Curran, L. Seaman, and D. A. Shockey, "Dynamic Failure of Solids," *Phys. Rep.*, **147**, 253–388 (1987).

[25]D. R. Curran, L. Seaman, T. Cooper, and D. A. Shockey, "Micromechanical Model for Continuum and Granular Flow of Brittle Materials under High Strain Rate Application to Penetration of Ceramic Targets," *Int. J. Impact Eng.*, **13**, 53–58 (1993).

[26]A. M. Rajendran, "Modeling the Impact Behavior of AD85 Ceramic under Multiaxial Loading," *Int. J. Impact Eng.*, **15**, 749–68 (1994).

[27]G. R. Johnson and T. J. Holmquist, "A Computational Constitutive Model for Brittle Materials Subjected to Large Strains, High Rates, and High Pressure"; pp. 1075–81 in *Shock Wave and High Strain Rate Phenomena in Materials*. Edited by M. A. Meyers, L. E. Murr, and K. P. Staudhammer. Marcel Dekker, New York, 1992.

[28]L. R. F. Rose, "Crack-Size Dependence of Fracture Toughness in Ceramic Polycrystals," *J. Mater. Sci. Lett.*, **5**, 455–56 (1986).

[29]L. R. F. Rose, "Effective Fracture Toughness of Microcracked Materials," *J. Am. Ceram. Soc.*, **69**, 212–14 (1986).

[30]B. Budiansky, J. Hutchinson, and A. G. Evans, "Matrix Fracture in Fiber-Reinforced Ceramics," *J. Mech. Phys. Solids*, **34**, 167–89 (1986).

[31]B. Budiansky, J. Amazigo, and A. G. Evans, "Small-Scale Crack Bridging and the Fracture Toughness of Particulate-Reinforced Ceramics," *J. Mech. Phys. Solids*, **36**, 167–87 (1988).

[32]D. B. Marshall and A. G. Evans, "Tensile Strength of Uniaxially Reinforced Ceramic-Fiber Composites," *Fract. Mech. Ceram.*, **7**, 1–15 (1986).

[33]D. B. Marshall, B. R. Lawn, and R. F. Cook, "Microstructural Effects on Grinding of Alumina and Glass-Ceramics," *J. Am. Ceram. Soc.*, **70**, C-139–C-140 (1987).

[34]D. B. Marshall and A. G. Evans, "Failure Mechanisms in Ceramic-Fiber/Ceramic-Matrix Composites," *J. Am. Ceram. Soc.*, **68**, 225–31 (1985).

[35]V. D. Krstic, "Grain-Size Dependence of Fracture Stress in Anisotropic Brittle Solids," *J. Mater. Sci.*, **23**, 259–66 (1988).

[36]A. G. Evans, "Fracture Characteristics of Ceramic-Matrix Composites"; p. 177 in *Flight-Vehicle Materials, Structures, and Dynamics—Assessment and Future*. ASME, New York, 1992.

[37]A. G. Evans, A. Bartlett, B. Davis, B. D. Flinn, M. Turner, and I. E. Reimanis, "Fracture Resistance of Metal/Ceramic/Intermetallic Interfaces," *Scr. Metall. Mater.*, **25**, 1003–10 (1991).

[38]A. G. Evans and B. J. Dalgleish, "Fracture Resistance of Metal–Ceramic Interfaces," *Acta Metall. Mater.*, **40**, S295–S306 (1992).

[39]W. A. Curtin, "Fiber Pull-Out and Strain Localization in Ceramic-Matrix Composites," *J. Mech. Phys. Solids*, **41**, 35–53 (1993).

[40]W. A. Curtin, "*In Situ* Fiber Strengths in Ceramic-Matrix Composites from Fracture Mirrors," *J. Am. Ceram. Soc.*, **77**, 1075–78 (1994).

[41]E. Y. Sun, P. F. Becher, K. P. Plucknett, C. Hsueh, K. B. Alexander, S. B. Waters, K. Hirao, and M. E. Brito, "Microstructural Design of Silicon Nitride with Improved Fracture Toughness," *J. Am. Ceram. Soc.*, **81**, 2821–40 (1998).

[42]B. R. Lawn, N. P. Padture, L. M. Bruan, and S. J. Bennison, "Model for Toughness Curves in Two-Phase Ceramics," *J. Am. Ceram. Soc.*, **76**, 2235–47 (1993).

[43]B. R. Lawn, "Indentation of Ceramics with Spheres, A Century after Hertz," *J. Am. Ceram. Soc.*, **81**, 1977–94 (1998).

[44]S. M. Wiederhorn, G. D. Quinn, and R. Krause, "Fracture Mechanism Maps: Their Applicability to Silicon Nitride," *ASTM STP*, **1201**, 36–61 (1994).

[45]S. M. Wiederhorn, G. D. Quinn, and R. Krause, "High-Temperature Structural Reliability of Silicon Nitride," *Key Eng. Mater.*, **89– 91**, 575–80 (1994).

[46]K. Niihara, A. Nakahira, and T. Sekino, "New Nanocomposite Structural Ceramics," *Mater. Res. Soc. Symp. Proc.*, **286**, 405–12 (1991).

[47]K. V. Logan, "Shaped Refractory Products and Method of Making the Same," U.S. Pat. No. 5 141 900, 1992.

[48]K. V. Logan, "Elastic–Plastic Behavior of TiB$_2$/Al$_2$O$_3$ Produced by SHS"; Ph.D. Dissertation. Georgia Institute of Technology, Atlanta, GA, 1992.

[49]Z. Bilek, J. Helesìc, J. Buchar, M. Kotoul, and V. Sìda, "Mechanical Properties of Aluminum Oxide at High Loading Rates," *Acta Tech. CSAV*, **35**, 741–53 (1990).

[50]R. Komanduri, "Advanced Ceramic Tool Materials for Machining," *Int. J. Refract. Hard Met.*, **8**, 125–32 (1989).

[51]C. E. Anderson and B. L. Morris, "The Ballistic Performance of Confined Al$_2$O$_3$ Ceramic Tiles," *Int. J. Impact Eng.*, **12** [2] 167–87 (1992).

[52]D. J. Viechnicki, M. L. Slavin, and M. I. Kliman, *Am. Ceram. Soc. Bull.*, **70**, 1035 (1991).

[53]A. F. Carney, "The Effect of Microstructure on the Mechanical Properties of a Titanium Diboride/Alumina Composite"; M.S. Thesis. Georgia Institute of Technology, Atlanta, GA, 1997.

[54]M. J. Edirisinghe, "Processing and Properties of Some Alumina–Boride Composites," *Mater. Res. Soc. Symp. Proc.*, **365**, 119–24 (1995).

[55]G. B. Kennedy, A. R. Keller, R. R. Russell, L. Ferranti, M. Zhou, and N. Thadhani, "Dynamic Mechanical Properties of Microstructurally Biased Two-Phase TiB$_2$ + Al$_2$O$_3$ Ceramics," *J. Appl. Phys.*, **91** [4] 1921–27 (2002).

[56]J. Zhai and M. Zhou, "Micromechanical Modeling of Mixed-Mode Crack Growth in Ceramic Composites"; pp. 174–200 in *Mixed Mode Crack Behavior*, STP 1359. Edited by K. Miller and D. L. McDowell. ASTM, New York, 1999.

[57]J. Zhai and M. Zhou, "Finite-Element Analysis of Micromechanical Failure Modes in Heterogeneous Brittle Solids," *Int. J. Fract.*, **101**, 161–80 (2000).

[58]J. Zhai, V. Tomar, and M. Zhou, "Micromechanical Modeling of Dynamic Fracture Using the Cohesive Finite Element Model, Part 1–Solution Convergence," *J. Eng. Mater. Technol.*, (2003), in review.

[59]J. Zhai, V. Tomar, and M. Zhou, "Micromechanical Modeling of Dynamic Fracture Using the Cohesive Finite Element Model, Part II—Numerical Simulations," *J. Eng. Mater. Technol.*, (2003), in review.

[60]J. Zhai, "Micromechanical Modeling of Dynamic Fracture in Ceramic Composites"; Ph.D. Thesis. Georgia Institute of Technology, Atlanta, GA, 2000.

[61]P. Follansbee, "The Hopkinson Bar"; pp. 198–203 in *Metals Handbook*, Vol. 8. American Society for Metals, Metals Park, OH, 1985.

[62]S. Nemat-Nasser, "New Frontiers in Dynamic Recovery Testing of Advanced Composites: Tailoring Microstructures for Optimal Performance," *JSME Int. J., Ser. 1*, **34** [2] 111 (1991).

[63]S. Nemat-Nasser, J. B. Isaacs, and J. E. Starrett, "Hopkinson Techniques for Dynamic Recovery Experiments," *Proc. R. Soc. London*, **435**, 371–91 (1991).

[64]A. R. Keller, "An Experimental Analysis of the Dynamic Failure Resistance of TiB$_2$/Al$_2$O$_3$ Composites"; M.S. Thesis. Georgia Institute of Technology, Atlanta, GA, 2000.

[65]D. E. Grady and M. E. Kipp, "Geometric Statistics and Dynamics Fragmentation," *J. Appl. Phys.*, **58**, 1210–22 (1985).

[66]D. E. Grady and M. E. Kipp, "Mechanisms of Dynamic Fragmentation: Factors Governing Fragment Size," *Mech. Mater.*, **4**, 311–24 (1985).

[67]D. A. Shockey, "Discussion of Mechanisms of Dynamic Fragmentation: Factors Governing Fragment Size," *Mech. Mater.*, **4**, 321–24 (1985).

[68]C. C. Lienau, "Random Fracture of a Brittle Solid," *J. Franklin Inst.*, **221** [1324] 485–94 (1936).

[69]N. F. Mott and E. H. Linfoot, *Ministry of Supply*, AC 3348 (1943).

[70]D. E. Grady, "Particle Size Statistics in Dynamic Fragmentation," *J. Appl. Phys.*, **68**, 6099–105 (1990).

[71]A. Nordgen and A. Melander, "Influence of Porosity on Strength of WC–10% Co Cemented Carbide," *Powder Metall.*, **31** [3] 189–200 (1988).

[72]V. D. Krstic, "Porosity Dependence of Strength in Brittle Solids," *Theor. Appl. Fract. Mech. II*, 241–47 (1988).   □